TENSION LIMIT OF FROZEN CLAY UNDER UNSTEADY LOADING AND TEMPERATURE CONDITIONS

Satoshi Nishimura[1, *], Masaki Tanaka[2] and Francesca Casini[3]

[1]Faculty of Engineering, Hokkaido University, Japan (*Corresponding author)
[2]Formerly Graduate School of Engineering, Hokkaido University, Japan
[3]Department of Civil Engineering and Computer Science, University of Rome Tor Vergata, Italy

ABSTRACT

The tensile strength characteristics of frozen clay was investigated by performing triaxial tension tests, in which the axial total stress was decreased to negative values while zero or positive lateral total stress was maintained. A particular focus is on the tensile strength against different loading rates, and more generally, against irregular loading and temperature changes. The test conditions involved insertion of loading pause(s), temperature increase, decrease or both, and variable loading rates. Different combinations of lateral stress and loading rate resulted in the strain at tensile failure ranging widely from around 1% to more than 20%. This variety of ductility has a significant bearing on Artificial Ground Freezing design. An interpretation framework adopting delayed tensile-degradation concept and temperature-dependent Tensile Failure Lines (TFLs) is proposed to describe the monotonic and non-monotonic loading/temperature tests altogether consistently. The only scenario that is not directly captured by this framework is cooling from relatively warm temperatures (-4°C in this study), which seemingly cancelled the degradation. While describing this scenario accurately still requires continued research, the proposed framework offers a platform for advanced numerical modelling incorporating tensile strength, as well as practical method for estimating the tensile failure from limited test data.

INTRODUCTION

The strength of frozen soils is a key design parameter in Artificial Ground Freezing (AGF), a geotechnical technique which exploits the increased strength, stiffness and decreased permeability of frozen soils in underground construction (e.g. Viggiani et al., 2015; Casini et al., 2023). There is currently no universally adopted code or de facto standard procedure for AGF stability assessment, but the design of frozen soil walls and shells usually involves assessing the shear and bending resistance against design loads (e.g. Izuta et al., 1988; Okubo et al., 2000). A typical example of bending-caused problems is the tensile stress appearing at the crown of frozen soil ring surrounding a tunnel (e.g. Jones and Brown, 1978; Jessberger, 1981). However, the stress analysis rarely adopts a mechanical model that describes tensile strength. Research into the tensile strength of frozen soils has been undertaken for decades (e.g. Eckardt, 1982; Akagawa and Nishisato, 2009;

Azmatch et al., 2011; Zhou et al., 2015; Yamamoto and Springman, 2017). Due to the inherently difficult nature of applying tension to soils accurately in laboratory, however, the tensile behaviour of frozen soils has been understood much less comprehensively than that in compression/shear (Li et al., 2025). This gap of knowledge, or worse, unwarranted extrapolation of our understanding of frozen soil behaviour in compression to that in tension hinders exploiting the full potential of AGF, because the very advantage of freezing soil lies in gaining a true tensile strength, which allows more flexible and economic design not possible in unfrozen ground.

The advantages and disadvantages of existing laboratory tensile testing methods were reviewed by Nishimura et al. (2023). The same work developed new triaxial 'tension' testing procedures in which, unlike in triaxial 'extension', a true negative normal stress was applied in the axial direction while confining stress remained on the radial direction. The tensile tests with various radial stresses revealed a new interpretive framework in which shear deformation and tensile failure interact. One of the representative stress-strain datasets from Nishimura et al. (2023) is replotted in **Figure 1**. Seeing that the peak deviator stress q increasing with the initial total mean principal stress (=radial stress during tension) in **Figure 1a**, one may be tempted to conclude that the peak resistance is determined by the lateral stress-dependent q, namely, by a total-stress-based *shear* strength criterion. However, all the samples were observed to fail clearly in tension, split across a horizontal (i.e. perpendicular to the tensile axis) rupture plane with mat, brittle texture once the peak resistance was mobilised, exhibiting an abrupt loss of resistance. Noting this eventual failure mode, the first author concluded that the strength criterion should be drawn with the tensile (i.e. axial) stress σ_a, shown as Tensile Failure Lines (TFLs) in **Figure 1b**.

The interpreted failure processes are schematised in **Figure 2**. The essence of this scheme is to envisage a tensile strength not as constant but degrading with the progress of shear deformation, as represented by the TFL. If soil is subject to tension while relatively large lateral stress (the major principal stress σ_1) exists, shear strength is first reached (the black curve). The peak resistance is therefore given by the limiting value of q. Even in this case, still, experimental observation revealed that the eventual failure mode at large strains involved brittle splitting along a horizontal plane, not shear sliding along a diagonal surface. It is natural to assume that the shear strain-induced damage to the soil structure facilitated tensile failure by effectively reducing the tensile strength along the TFL. In contrast, when the tension occurs with small or no σ_1, the tensile strength is reached before the q-limit (the grey curve). Assuming the steadily decreasing tensile strength in form of the TFL explains why simply compiling the peak q or σ_3 values at failure does not lead to consistent understanding of the resistance in tension under general conditions. The same scheme is successful in explaining all the results for clay samples with different pre-consolidation pressures and temperatures (Nishimura et al., 2023).

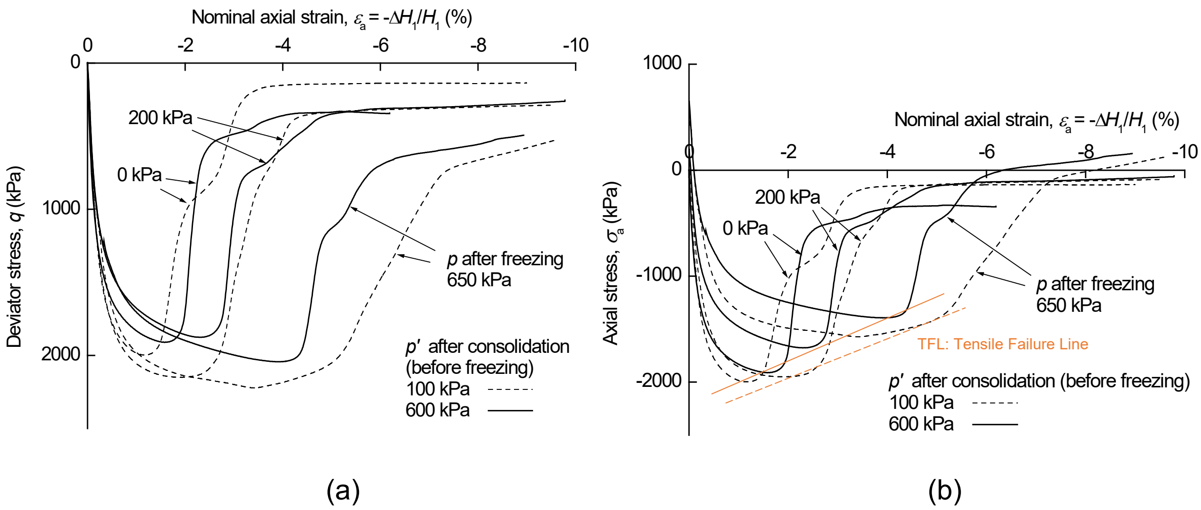

Figure 1: Representative results from monotonic triaxial tension tests on frozen Kasaoka clay at -9°C (Nishimura et al., 2023) (a) Deviator stress q, (b) Tensile (axial) stress σ_a (p and p' are total and effective mean effective principal stresses, and H_1 will be defined later in Figure 3)

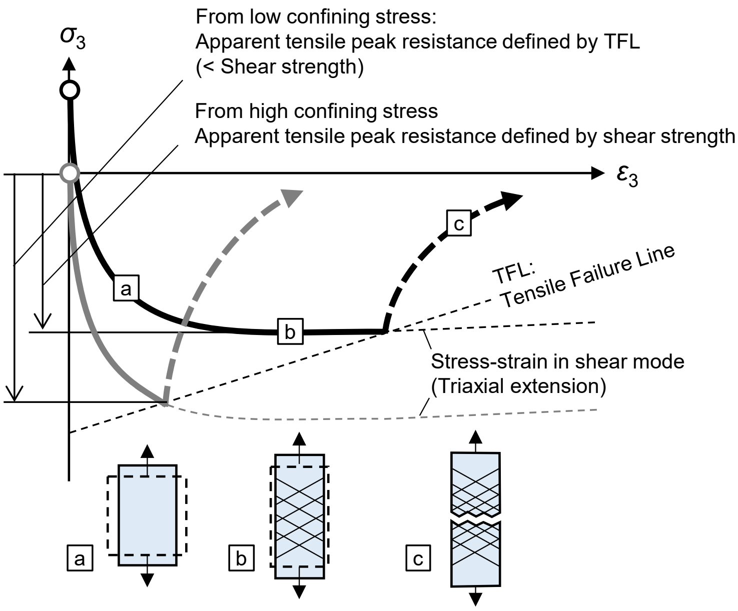

Figure 2: Schematic explanation of tensile failure processes with TFL (σ_3 and ε_3: Minor principal stress and strain, respectively. the tensile rupture exploiting diagonal shear planes was actually observed experimentally; see Nishimura et al., 2023)

The previous work also left assignment for future research. Applicability of the above TFL framework to different loading rates, and more generally, unsteady loading conditions involving irregular changes of strain rate and temperature needs to be tested. Take the issue of loading rate effect – existing studies report somewhat counter-intuitive results. For example, Azmatch et al. (2011) showed that faster loading could lead to both smaller or greater tensile resistance in their beam-bending experiments on frozen silt. The unconfined direct tension tests by Zhu and Carbee (1985; 1987) on frozen silt show greater ductility (i.e. greater strain at failure) for faster loading – as opposed to what is observed in compression (e.g. Parameswaran, 1980; Xu et al. 2017). When irregular loading is involved, Zhou et al. (2017) showed that allowing longer strain pauses and hence longer stress relaxation during loading in frozen loess led to greater eventual compressive strength, possibly due to recrystalisation of pore ice during the loading pauses. On the contrary, Wang et al. (2017) showed that shear stress-strain relationships in frozen clay followed patterns uniquely define for a given temperature, not affected by significantly long (24-hour) stress relaxation. As these examples suggest, irregular loading effects are not consistently understood even for compression, and much less for tension. The difference of strength characteristics between tension and compression mentioned above might reflect a potential difference in the microscopic mechanisms. Tension may eventually be sustained only by ice bonding, while compression may be resisted more by soil grain-to-grain shearing until the end. However, the experimental data available at the moment are too unsystematic to support such speculation. While creep models in compression/shear have been increasing refined to take account of irregular loadings (e.g. Schindler et al. 2025), almost no experimental data that allows the same for tensile behaviour has been accumulated.

This paper continues with the experimental programme initiated by Nishimura et al. (2023) to address the tensile characteristics of frozen clay under more general loading patterns involving constant or irregular strain rates and temperatures. A significant number of tests have been conducted in three years since the above first report, allowing the authors to propose a prototype of framework to consistently explain the frozen clay's tensile limit for a variety of scenarios. It will be clearly demonstrated that the tensile strength is not uniquely determined by the contemporary strain rate and temperature but affected by history, which seemingly influences the subsequent behaviour with some delay. The implications of the findings to AGF practice will also be briefly discussed.

MATERIAL AND TESTING METHOD

Material

Reconstituted Kasaoka clay was tested. The clay and its preparation procedures were same as Nishimura et al. (2023). The clay had the liquid limit: 60-62%, the plastic limit: 28%, the clay fraction (<2μm): 40%, and the particle density: 2.65Mg/m^3. The sample was preconsolidated one-dimensionally from slurry to 100kPa in a 220mm-diameter consolidometer. Single consolidated clay cake provided 9 test specimens. The clay was trimmed into a dumbbell shape, illustrated and photographed in **Figure 3**. The diameter was 50mm in the top and bottom flanges (D_1), and 30mm in the middle (D_2). This shape concentrates the axial stress to the middle part, and successfully forced the rupture failure to occur there without inducing detachment of the specimen ends from the stainless-steel platens, where the tensile force transfer was solely achieved through the freeze adhesion. The end detachment occurred only in cases involving a soil temperature of -15ºC and a fast axial strain rate of 1%/min. It appears that the freeze adhesion strength does not increase with a temperature decrease and loading rate increase in proportion with the tensile strength. Such cases would have required smaller D_2/D_1, and were eventually given up in this study. The trimmed surface of the middle straight part was at least 20mm away from the consolidometer wall, where the friction may have caused stress non-uniformity. The water content was 45.64$\pm$0.26% in the cut specimens, indicating good uniformity.

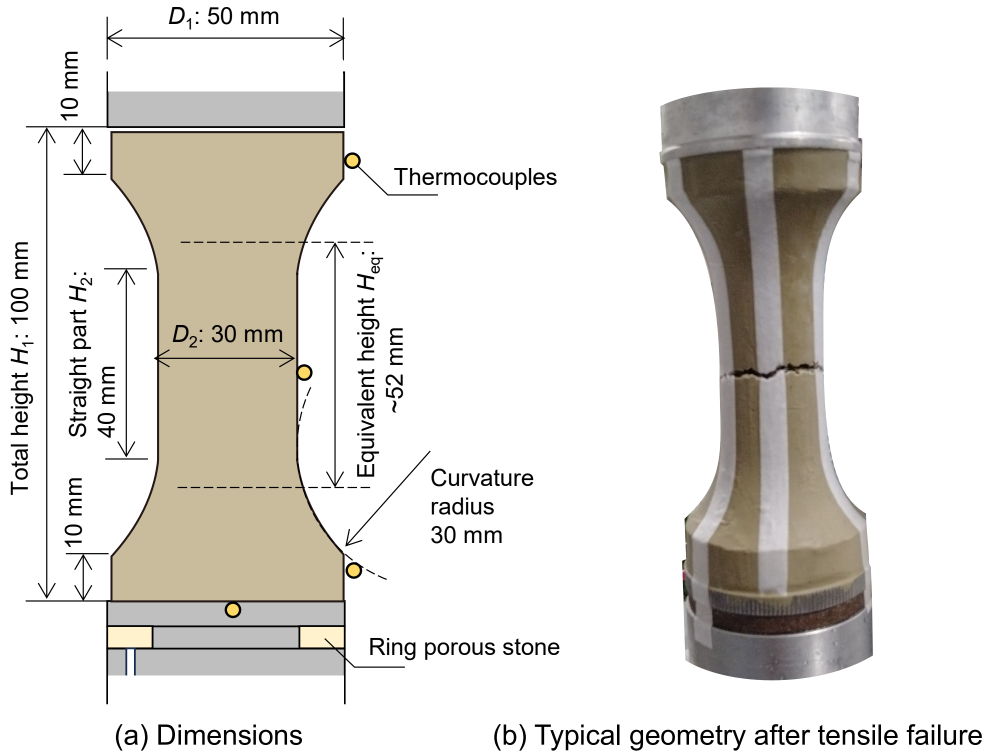

Figure 3: Geometry of test specimen and equivalent height H_{eq}

Testing apparatus and method

The same apparatus as described by Nishimura et al. (2023) was used for triaxial tension tests in this study. The triaxial pressure cell houses acrylic inner cylinder walls surrounding the specimen. The refrigerant (ethylene glycol) cooled by an auxiliary cooling bath was circulated between this inner wall and the specimen's outer surface. This direct contact between the specimen and the refrigerant flowing in a restricted space allowed efficient and swift control of the specimen temperature.

The adopted procedures leading up to the triaxial tension stage followed those in the earlier work. As the technical details of the apparatus and the techniques are described by the above paper, only a brief report is given below. The trimmed sample was placed in the triaxial cell and consolidated isotropically to the effective stress p_c' of 100 or 200kPa, with the back pressure of 100kPa, in the room temperature of 24°C. It was then frozen in the triaxial cell directly after being consolidated, without releasing the cell pressure. This was achieved by exchanging the cell water with refrigerant pre-cooled at -27°C while air supply compensating for any pressure variations caused by the cell fluid removal/injection. The undrained conditions and isotropic stress state were maintained during freezing. The time taken in complete freezing, as suggested by the stop of axial displacement, was about 20 minutes. This freezing process was quick enough not to develop any visible ice lenses and cracks associated with internal water migration. The freezing can be controlled either as from bottom upwards (i.e. one-dimensional) or from all around, by regulating the refrigerant level rise during freezing. The latter approach was adopted here, as an earlier investigation (Nagai and Nishimura, 2020) did not show significant difference in the post-freezing shear behaviour in a cylindrical specimen. Given the geometry, the middle part that is to eventually fail in tension was frozen predominantly in the radial direction. This part is far from the flanges, which may be subject to more complex and hence unknown stress development by freezing. After about 1 hour of rest, the specimen temperature was raised to specified temperature T (-4, -9 or -15°C). The total stress was changed, if necessary, to a specified value p_{f} (0, 200, 300 or 650 kPa) after half a day. The tension was then applied by raising the axial loading ram while keeping the radial stress $\sigma_r = p_{\mathrm{f}}$. The conditions for the subsequent axial control and temperature for all the test cases are described subsequently.

Strain calculation

The strains due to consolidation were calculated based on the volume change and the axial displacement, assuming that the strains were uniform across the specimen against isotropic loading. The strains due to undrained freezing were calculated similarly. The volume change due to pore water phase changes was estimated based on the clay's freezing curve (unfrozen water content w_u– temperature T relationship) (Wang et al., 2017).

The earlier work (Nishimura et al., 2023) presented the nominal axial strain during tension as the global axial displacement ΔH_1 divided by the specimen total height H_1 (see **Figure 1**), while the axial stress was calculated by dividing the axial force by the middle cross-section area $\pi D_2^2/4$. For element modelling purposes, however, more precise estimation of strain in the mid-height part is desired, given that the rupture failure always occurred there. This was done in this study by estimating the equivalent height H_{eq}, by which the middle-part axial strain is expressed as

$-\Delta H_1/H_{\mathrm{eq}}$ (tensile strain as negative). This study adopts H_{eq}=0.52H_1, based on the analysis illustrated in Appendix. In reporting the axial strain ε_{a}, this paper uses the H_{eq} value at the start of tension (i.e. Cauchy strain). Similarly, the axial stress σ_{a} reported in this paper is the axial force divided by the post-freezing, pre-tension value of $\pi D_2^2/4$, without updating it during tension.

Testing conditions

This paper analyses a total of 43 tests, of which 7 are cited from Nishimura et al. (2023) and 36 were newly performed. They are grouped into three series, A-C, as shown in **Tables 1-3**, respectively. Series A contains monotonic tension tests with three different, constant temperatures T (-4, -9, and -15°C) and three different axial strain rates $\dot{\varepsilon}_a$ (0.01, 0.1 and 1%/min; the minus sign will be omitted for the rate). All but four cases were performed on samples consolidated at p'_{c}=100kPa. The four cases were performed with p'_{c}=200kPa and used as reference for Series B, which adopted constant confining stress p_{f} and constant strain rate but with a 4-hour loading pause and reloading. The strain was kept constant and stress relaxation was allowed while the temperature was changed from T_1 to T_2 during this pause. This was followed by loading resumption at T_2. This loading scheme is illustrated in **Figure 4**. Series C contains miscellaneous cases, in which more irregular conditions were applied. Each case in Series C will be explained as its result is presented. For all the tests, the applied pre-freezing back pressure was 100kPa.

Table 1: Conditions for monotonic tension tests (Series A)

	Case name	Effective (pre-freezing) consolidation stress p'_{c} (kPa)	Temperature T (°C)	Final total confining stress p_{f} (kPa)	Axial strain rate $\dot{\varepsilon}_a$ (%/min)
Series A: 24 Tests[1)]	A($-T$)-(p_{f})-($\dot{\varepsilon}_a$) (e.g. A4-200-0.1)	100	-4, -9	0, 200, 650	0.01, 0.1, 1
		100	-15 [2)]	200	0.01, 0.1
		200	-4, -9, -15	300	0.1
		200	-15	300	0.01

[1)] 7 tests from Nishimura et al. (2023)

[2)] The set with T=-15°C lacks $\dot{\varepsilon}_a$=1%/min cases, as they repeatedly suffered specimen-platen detachment during tension.

Table 2: Conditions for non-monotonic tension tests (Series B)

	Case name	1st-phase Temperature T_1 (°C)	Axial strain at pause $\varepsilon_{\mathrm{ap}}$ (%)	2nd-phase Temperature T_2 (°C)	Other
Series B (14 Tests)	B$(-T_1)$-$(-\varepsilon_{\mathrm{ap}})$-$(-T_2)$ (e.g. B9-2%-4)	-4	-2	-4, -9, -15	p'_{c}=200kPa
		-4, -9, -15	-4	-4, -9, -15	p_{f}=300kPa
		-4	-8	-9, -15	$\dot{\varepsilon}_a$=0.1%/min

Table 3: Conditions for irregular loading tests (Series C)

	Case name	Description	Other
Series C (5 Tests)	C9-4%4-9	Similar to B9-4%-9 but T was raised to -4°C once and lowered again to -9°C during loading pause	p'_{c}=200kPa p_{f}=300kPa $\dot{\varepsilon}_a$=0.1%/min
	C15-300-SD	Similar to A15-300-0.05 but slowed down from 0.1%/min to 0.02%/min after ε_{a}=-4%	
	C9-300-MP	T= -9°C. 4-hour pauses were applied at ε_{a}=-1.7, -4.5 and 7.5%	
	C9-200-SU	Similar to A9-200-0.01 but speeded up from 0.01%/min to 0.1%/min after ε_{a}=-2%	p'_{c}=100kPa p_{f}=200kPa
	C9-200-VS	T= -9°C. $\dot{\varepsilon}_{\mathrm{a}}$ was varied stepwise between 0.01, 0.1, and 1%/min randomly; see **Figure 12**.	

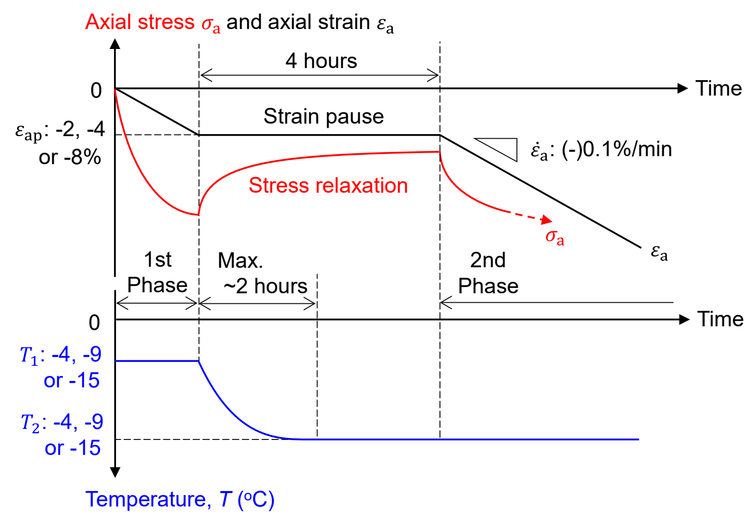

Figure 4: Control scheme of Series B tests

EFFECTS OF STRAIN RATE AND HISTORY ON TENSILE FAIURE UNDER CONSTANT TEMPERATURE

Constant strain-rate cases

The results from Series A tests allow simple comparison of tensile resistance against different constant strain rates under different constant temperatures. The axial stress-strain curves are shown in **Figure 5(a)-(c)** for each temperature. The overall trend is clear – lower temperature and greater strain rate lead to greater tensile resistance (i.e. smaller σ_{a}), as have been known from Zhu & Carbee (1985; 1987). The strain to failure also increases with the strain rate increase. This is less intuitive, since compression tests tend to show the opposite trend (e.g. Xu et al., 2017). However, similar results had been reported again by Zhu & Carbee (1985; 1987) in their unconfined direct tension tests, and this study confirms this peculiar feature of increased ductility for faster loading for frozen soils under tension with more general radial stress, σ_{r}, conditions. The effect of all the three factors – temperature, strain rate and radial stress – is significant. Depending on the combination of the three factors, tensile failure may be reached within ε_{a}=-1% to -2% or may not be reached even by ε_{a}=-20%. This potential difference in ductility can be significant enough to affect the engineering decision in AGF.

As illustrated in **Figure 5**, a family of envelopes representing tensile rupture failure can be visualised for each strain rates. As far as we stick to the authors' earlier theory of shear-tension mechanism, the $\sigma_{\mathrm{a}}:\varepsilon_{\mathrm{a}}$ relationship initially follows that of shear deformation (triaxial extension) as influenced by strain rate. If it attains the peak shear resistance before reaching tensile failure, the minimum value of σ_{a} is determined by the rate-dependent shear strength q_{max}, as $\sigma_{\mathrm{a}} = \sigma_{\mathrm{r}} - q_{\mathrm{max}}$. **Figure 6** shows q_{max} against the axial strain rate in Series A. The strain rate-dependency of the shear strength of same frozen Kasaoka clay was studied in triaxial compression by Wang et al. (2017). By taking $\dot{\varepsilon}_a$=0.1%/min as reference, they observed that the shear strength increased by 9.2% per $\log_{10}$ cycle in compression, as indicated as broken lines in the figure. This rate-dependency generally applies to the results of tension here. In closer look, however, the data at $\dot{\varepsilon}_a$=0.01%/min tend to lie slightly below the trend line. This is because the stress-strain curves tended to hit the TFL before fully mobilising the shear strength in slower loading. The lack of resistance plateau is clear for the cases with $\dot{\varepsilon}_a$=0.01%/min in **Figure 5**, indicating the deformation cut short by tensile failure. For such cases, the peak resistance is given by the TFL. In the faster loading cases, on the contrary, the peak resistance is given by the shear strength q_{max} and its strain rate-dependency. TFL is still relevant, however, as it determines that deformable limit (length of the plateau).

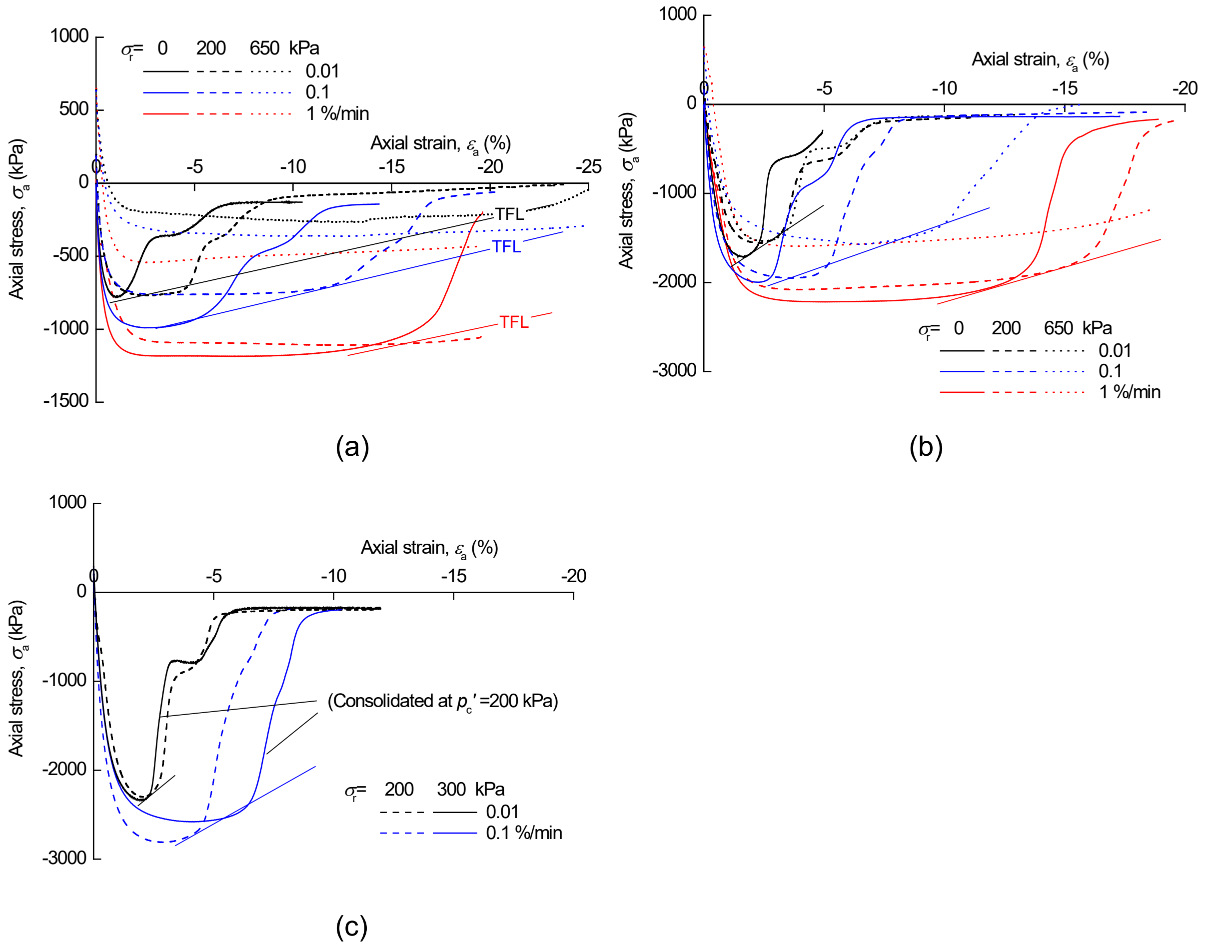

Figure 5: Axial stress-strain relationships during monotonic tension in Series A: (a) T=-4°C, (b) T=-9°C tests, (c) T=-15°C

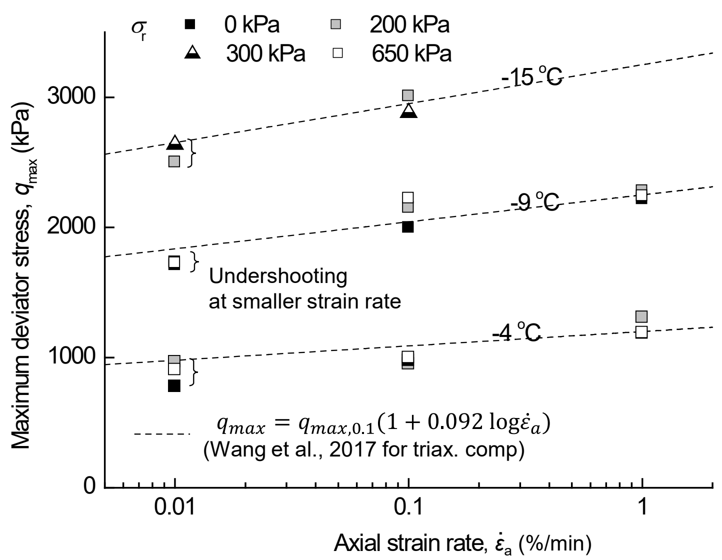

Figure 6: Peak deviator stress in Series A ($q_{max,0.1}$: q_{max} at $\dot{\varepsilon}_a$=0.1%/min)

Cases with loading pauses

The above observation leads to an idea of combining a visco-plastic constitutive model describing the strain-rate-dependent shear behaviour with a temperature-, strain- and strain-rate-dependent TFL for complete description of frozen soil behaviour under tensile loading. However, this idea faces a problem when the cases with loading pause in Series B are considered. **Figure 7** shows the axial stress- strain relationships from the tests in which 4-hour loading pauses were given at different strains, without any change in the temperature. When the loading was resumed with the same, original strain rate (0.1%/min), the stress soon recovered to the pre-pause level. However, the interruption clearly led to earlier onsets of tensile failure. This is so, even though no deformation was allowed during the pause while the axial tensile stress was allowed to relax. The greater the strain at which pause occurred, the earlier the onset of tensile failure was. This phenomenon cannot be explained by the TFL set uniquely to temperature, strain and strain-rate (e.g. the isotherm isotach concept by Kochi et al., 2025); these three factors are all same at Points a, b and c in **Figure 7(a)**. While an isotach approach may still be adopted for the pre-tensile failure shear process (Wang et al., 2017), considering the history in another manner is required for the later, tensile failure process.

The pre-pause stress-strain behaviour was generally repeatable in these tests, but not perfectly. For example, the stress-strain curves of B9-4%-9 showed a resistance plateau at relatively small strain (~2%), and the early tensile failure might reflect not just the loading pause influence but also test variability. Despite the uniformity of water content in the preconsolidated specimens described earlier, factors of variability may have been introduced by subsequent processes. The tensile failure is brittle and unstable by nature, affected by small perturbations – the imperfect alignment of apparatus-specimen axes may be one of the factors, giving rise to a small moment. Even allowing for potential test variability, however, the influence of loading pause is clear. Interestingly, Zhou et al. (2017) report opposite behaviour for frozen loess in compression, showing that insertion of loading pauses alleviates strain-softening. This was attributed to pore ice recrystalisation during loading pauses. In tension, however, defect propagation under a prolonged tensile stress regime seems more dominant.

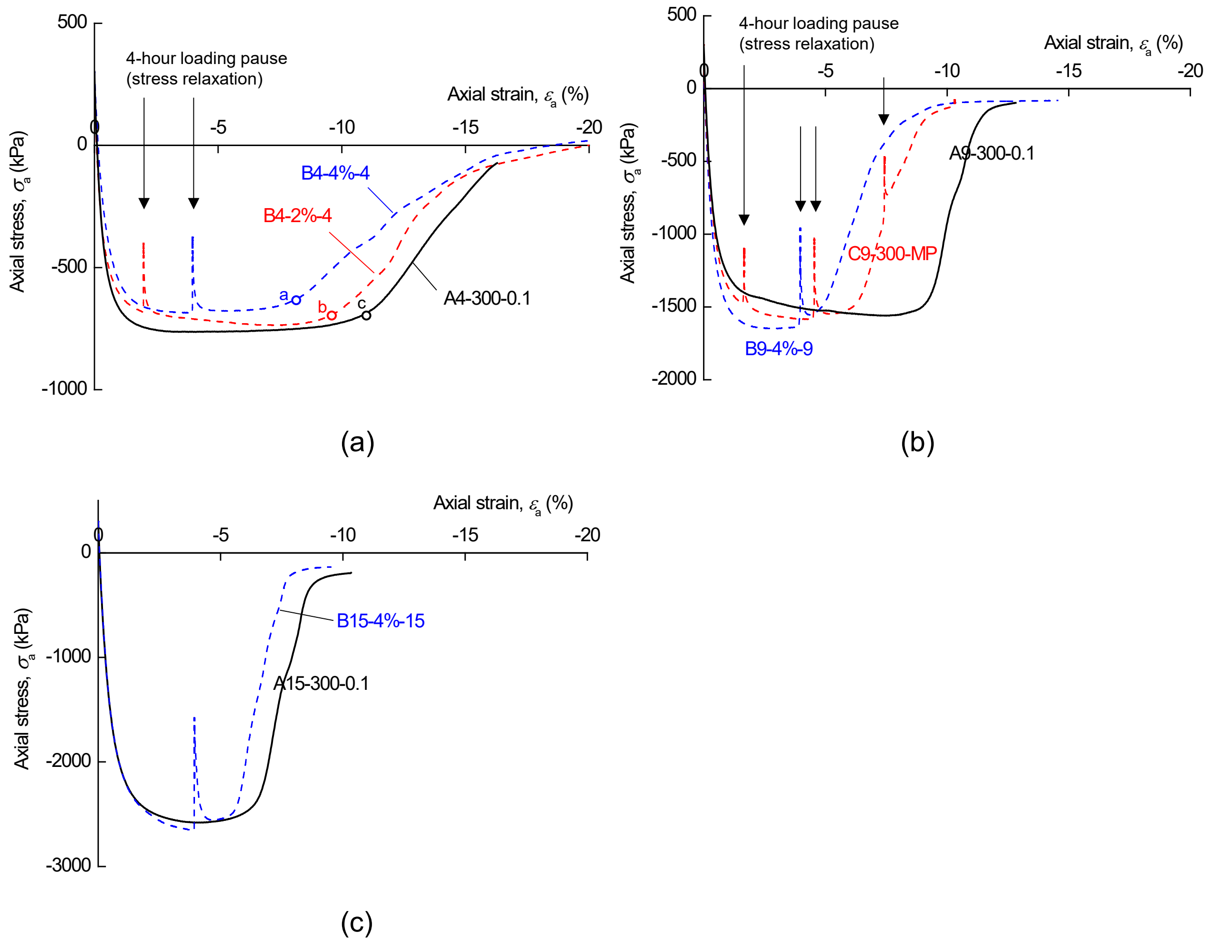

Figure 7: Influence of loading pauses observed in Series A and B: (a) T=-4°C, (b) T=-9°C tests, (c) T=-15°C

Delayed tensile-degradation concept

Observation of the loading pause effect led the authors to seek a new approach to describing the occurrence of tensile failure. Noting the correlation of the tensile strength with shear work input for monotonic loading cases indicated by Nishimura et al. (2023), this study explored the applicability of shear work-based tensile failure criterion. To consider the effect of strain rate, loading pauses, and any strain history in general, it is postulated that the shear work input at given time is fully converted to the effective internal damage on tensile strength with some time delay. The idea combines some elements of damage mechanics models (e.g. He et al., 2000; Xu et al., 2015), visco-plasticity and double-hardening models (i.e. separate evolution in shear and tension resistances), while not aligning strictly with any of these.

As the volumetric deformation is negligible in saturated frozen soil, the total work input per unit volume over a finite short period ΔW by triaxial loading comes only from shear:

$$\Delta W = \sigma_{\mathrm{a}}\Delta\varepsilon_{\mathrm{a}} + 2\sigma_{\mathrm{r}}\Delta\varepsilon_{\mathrm{r}} = (\sigma_{\mathrm{a}} - \sigma_{\mathrm{r}})\Delta\varepsilon_{\mathrm{a}} = -q\Delta\varepsilon_{\mathrm{a}} \tag{1}$$

The minus sign is for tension, where $q = \sigma_r - \sigma_a$. It is assumed, in analogy with the Arrhenius equation, that this input is converted to 'effective' work ΔW^* in the ensuing time by the following function:

$$d(\Delta W^*(\tau, t))/d\tau = \Delta W(t) a e^{-a\tau} \tag{2}$$

Where t is the time of ΔW input, τ is the time after t, and a is a decay parameter. After sufficient time ($\tau \to \infty$), the work input is fully converted to ΔW^*:

$$\Delta W^*(\infty, t) = \int_0^\infty [d(\Delta W^*(\tau, t))/d\tau]\, d\tau = \Delta W(t) \tag{3}$$

For any irregular loading history, the total effective work $W^*(t_1)$ at current time t_1 is calculated by integrating Eq.(2) with regard to τ from 0 to $t_1 - t$, and with regard to t over infinite past ($-\infty$) to now (t_1), as W^* at any time is influenced by ΔW from infinite past;

$$W^*(t_1) = \int_0^{t_1 - t} \int_{-\infty}^{t_1} (-q\dot{\varepsilon}_{\mathrm{a}}) a e^{-a\tau} d\tau\, dt \tag{4}$$

This scheme is shown in **Figure 8**. In general, this computation requires memory of the entire previous loading history, which would pose inconvenience in implementing the concept to numerical analysis of irregular loading. When the exponential decay function $ae^{-a\tau}$ is adopted, however, some mathematical operation leads to the following, history-independent relationship:

$$\dot{W}^*(t) = a\big(W(t) - W^*(t)\big) \tag{5}$$

where $W(t)$ is the cumulative shear work. Eq. (5) can be input to finite time-difference computation by keeping record only of the cumulative values of W and W^*. Different choice of decay function may be possible to represent the process phenomenologically better, but this mathematical feature offers great convenience. **Figure 9** shows examples of $\sigma_{\mathrm{a}}: W^*$ relationships for the T=-9°C cases in Series A. The parameter a was calibrated as 7.0×10^{-5} 1/sec (meaning that 50% of the total work is converted to the effective work in 9,902sec, and 90% in 32,893sec). Note that the tensile failure points are taken as the stress-strain curves' inflection points, and do not necessarily appear as inflection points in the $\sigma_{\mathrm{a}}: W^*$ plot. The tensile failure points are aligned narrowly along a single curve, regardless of the initial confining stress and strain rate. **Figure 10(a)** shows the tensile failure points for three different temperatures T=-4, -9 and -15°C, obtained in a similar manner from the monotonic loading tests in Series A. Despite some outliers, a broadly unique relationship is seen for each temperature, as long as the temperature remains constant. These relationships will be redefined as Tensile Failure Lines (TFLs) hereinafter, and used as reference for discussion of non-monotonic cases. The TFLs collapse into a single curve when normalised by the σ_a-intercept, as shown in **Figure 10(b)**. Note that the a value was calibrated here by using only the monotonic tests from Series A, with constraints such that a is unique regardless of the temperature, and that the data points cluster along three TFLs with least scatter. The initialisation of W^* was done after freezing under isotropic stresses and before the application of deviator stress.

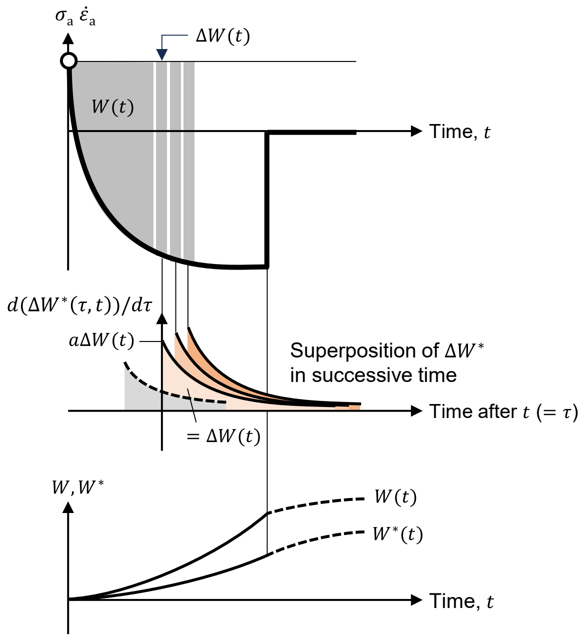

Figure 8: Concept of delayed accumulation of effective work

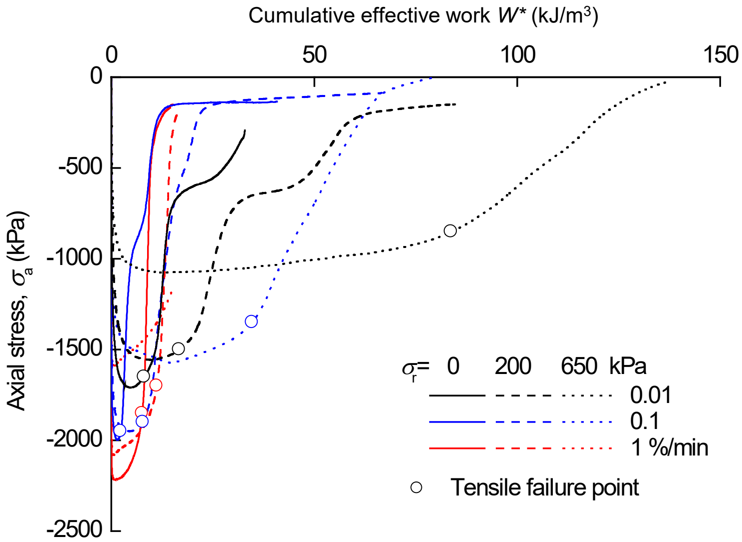

Figure 9: Tensile failure points in axial stress-effective work relationship: Example of T=-9°C

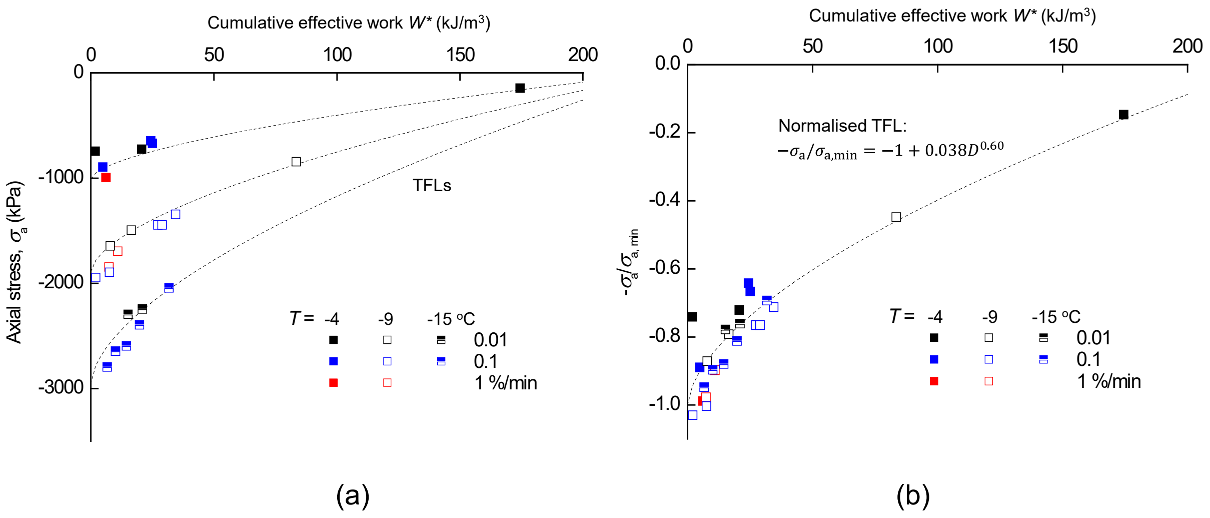

Figure 10: Tensile failure points and Tensile Failure Lines (TFLs) in monotonic loading tests in Series A: (a) For each temperature T, (b) Normalised ($\sigma_{a,min}$: σ_a at W^*=0)

The σ_a: W^* relationships in Series B with loading pause(s) under constant temperature are compared with those from the monotonic loading cases from Series A for each temperature in **Figure 11**. The effective work W^* accumulated even during the loading pauses, to catch up with the work input W according to Eq. (5). This scheme explains why the pause at ε_a=4% leads to earlier tensile failure than that at ε_a=2% (**Figure 7(a)**). The W^* value corresponding to the work input up to ε_a=4% is greater, and this brings the state closer to the TFL after the loading pause and stress relaxation, as shown in **Figure 11(a)**. Although the same mechanism is at work for the other temperatures, the reloading after the loading pause at T=-9°C and -15°C exhibited significant over-shooting of the TFL. However, this over-shooting was only temporary – the axial stress swiftly bounced back to values above the TFL, without showing any stress-strain plateau. Such over-shooting was also observed in another type of non-monotonic loading reported by Nishimura et al. (2023). The mechanism for this temporary over-shooting is unknown, but has been recognised for other unfrozen geomaterials too when they are subject to sudden loading acceleration (e.g. Tatsuoka et al., 2002). The TFL should be understood not as a tensile resistance upper bound, but a boundary between stable and unstable states.

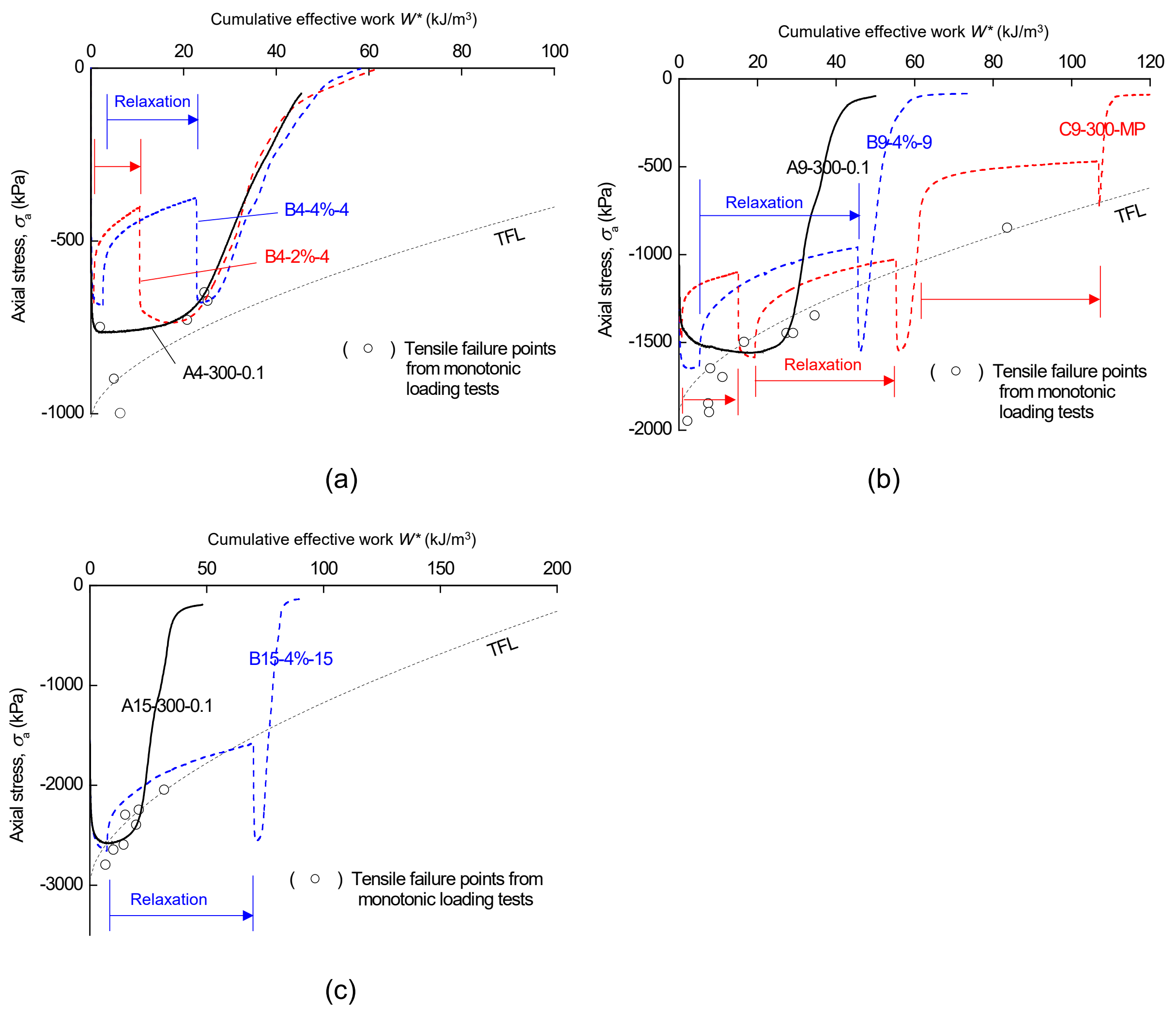

Figure 11: Axial stress-effective work relationships in tension with or without loading pauses (stress relaxation): (a) T=-4°C, (b) T=-9°C tests, (c) T=-15°C

Similar $\sigma_a : \varepsilon_a$ and $\sigma_a : W^*$ plots are shown for the other irregular loading cases at T=-9°C in **Figure 12**. Case C9-200-SU involved speeding up the axial strain rate from 0.01%/min to 0.1%/min at ε_a=-2%. Case C9-200-VS was run with three different rates of 0.01, 0.1 and 1%/min, applied at irregular strain intervals. These two tests exhibit somewhat smaller resistance before the conditions parted from each other by 1.6-2.7% than the monotonic case A9-200-0.1, suggesting sample variability. C9-200-SU, starting with the slower rate of 0.01%/min, is supposed to fail in tension at a smaller strain than A9-200-0.1 according to the above theory (because of greater W^* accumulation at initially slower loading), but the inherently weaker nature of the C9-200-SU specimen apparently provided a room for developing greater strain before meeting the TFL. The fact that the whole test series were performed by two different operators over three years poses difficulty in attaining perfect repeatability. However, allowing for the limitation of precision in defining the TFLs in **Figure 10**, It is fair to consider that the $\sigma_a : W^*$ relationships under a variety of different loading conditions abide by the TFLs.

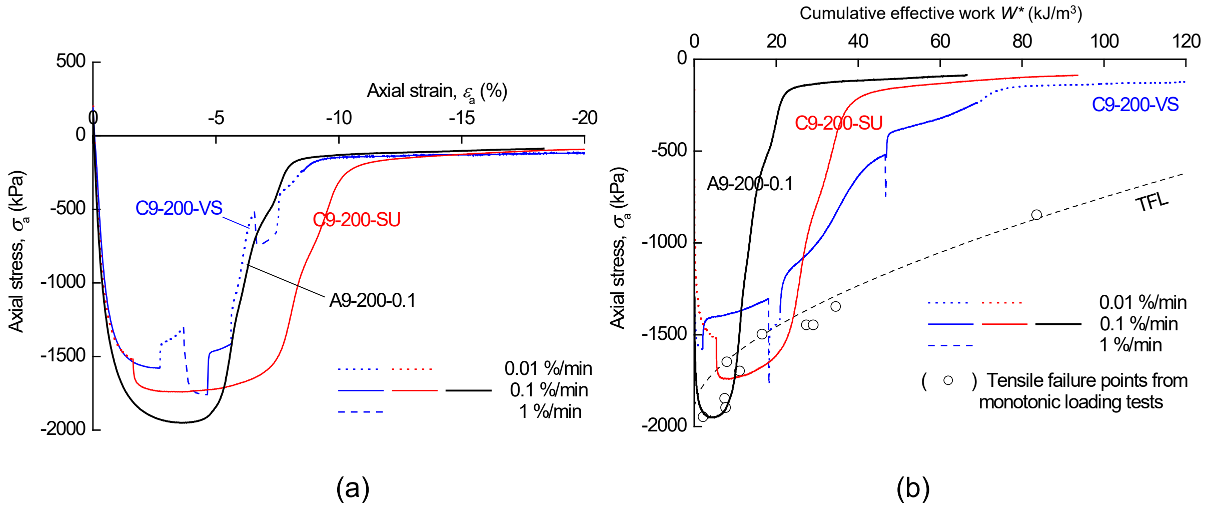

Figure 12: Tensile behaviour in irregular loading cases at *T*=-9°C (with the monotonic loading case A9-200-0.1 shown for reference): (a) Axial stress-strain, (b) Axial stress-effective work

Figure 13 shows the result of C15-300-SD, in which the axial strain rate was slowed down at around the peak resistance, compared with the monotonic test A15-300-0.1. The slowdown led to immediate increase of σ_a, bringing the path away from the TFL. The TFL was not approached again by the loading at smaller rate, possibly because the tensile mechanism had already been formed at around the σ_a peak.

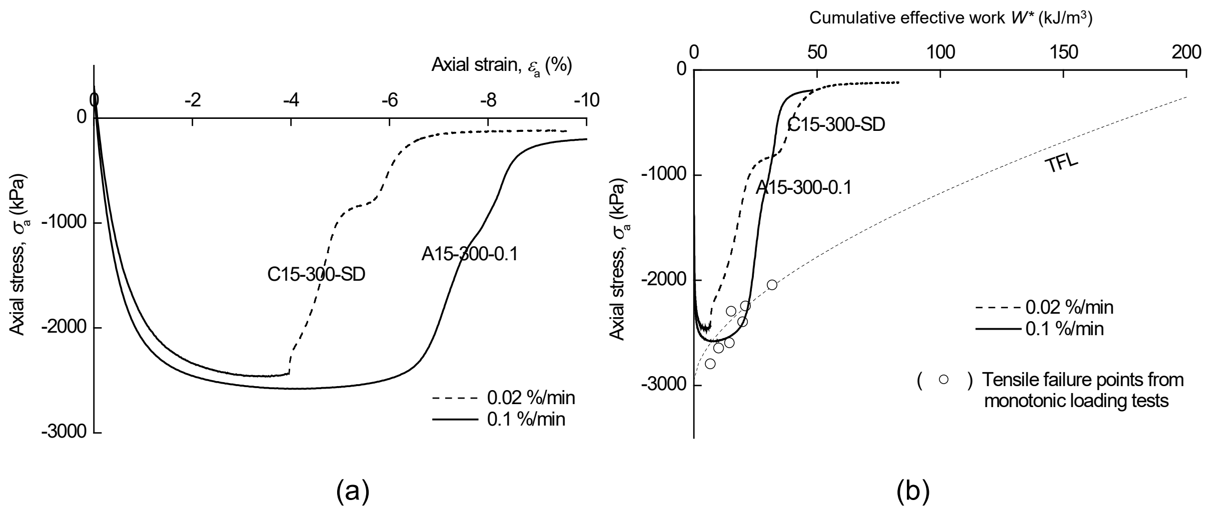

Figure 13: Tensile behaviour in irregular loading cases at *T*=-15°C (with the monotonic loading case A15-300-0.1 shown for reference): (a) Axial stress-strain, (b) Axial stress-effective work

EFFECT OF TEMPERATURE CHANGES ON TENSILE FAILURE

Temperature increase (warming) cases

The axial stress-strain relationships from the three Series B cases in which the temperature was increased (i.e. the 'warming' cases) during the loading interruption are shown in **Figure 14**. Significant stress relaxation occurred during the temperature change over 4 hours, and the effective work W^* accumulation during this period led to decreased tensile strength for reloading. The second loading phase with increased temperature broadly obeys the TFLs for respective temperatures, although the B15-4%-9 specimen had shown a sign of earlier tensile failure before reaching ε_a=-4%, and this may have led to the $\sigma_{\rm a}:W^*$ path in the second phase loading falling slightly short of the TFL. Generally, however, the proposed scheme seems to work with the warming cases.

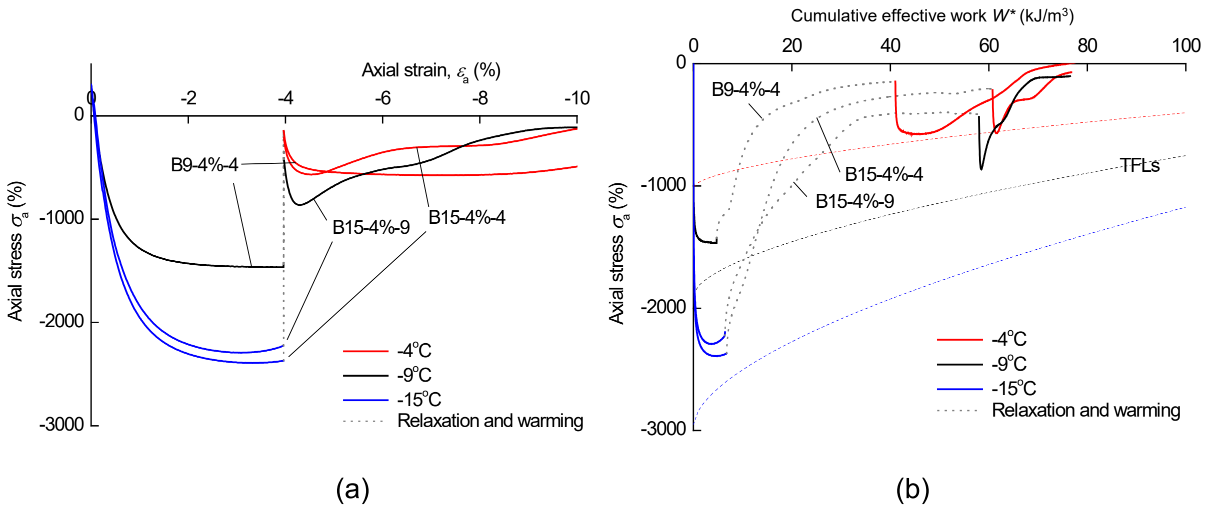

Figure 14: Tensile behaviour in cases where warming occurred during loading pause: (a) Axial stress-strain, (b) Axial stress-effective work

Temperature decrease (cooling) cases

The Series B cases in which the temperature was decreased (the 'cooling' cases) are considered here in the same manner. **Figure 15** shows the cases in which the first-phase temperature was -4°C. The cooling led to significant increase in the resistance against the second-phase loading. The slightly smaller peak resistances in B4-4%-15 and B4-4%-9 are likely to be due to the initial sample variability, as these correspond to the first and second weakest samples at ε_a=-2%, respectively, the strain below which all the six tests had a same condition. The $\sigma_{\rm a}:W^*$ paths reveal that the TFLs are not working as the tensile failure criteria. Even allowing for uncertainty of the exact TFL locations due to data scattering in **Figure 10**, the deformation continued well after the first engagement of the TFLs, as most clearly seen in B4-8%-9 and B4-8%-15. The stress-strain curves in **Figure 15(a)**, once the inherently weaker nature of the B4-4%-9 and B4-4%-15 samples is taken into account, suggest that cooling completely revives the tensile resistance, bringing the soil to fresh state; also note that their peak resistance is comparable to the monotonic case A15-300-0.1 shown in **Figure 13**.

Noting this 'healing' effect, the $\sigma_{\mathrm{a}}: W^*$ relationships for the post-cooling, second phase were recalculated by resetting W and W^* to zero prior to the loading resumption, as shown in **Figure 15(c)**. In this manner, the paths are compatible with the TFLs. The results from the cooling cases from -9°C (B9-4%-15) can be discussed similarly by following the same format, as shown in **Figure 16**. Although the cooling to -15°C provided extra tensile strength, the effect seems ephemeral; σ_{a} rebounded soon, suggesting immediate tensile failure upon the second loading. In this case, replotting the second-phase $\sigma_{\mathrm{a}}: W^*$ relationship by resetting W and W^* to zero, shown in **Figure 16(c)**, does not work well, with the path falling far short of the TFL.

C9-4%4-9 is a special case in which the temperature was first increased from -9°C to -4°C and then decreased back to -9°C at ε_{a}=-4%. The second loading after this operation led to clear over-shooting of the TFL. The W and W^* reset due to cooling works in this case, with the second-phase path in **Figure 16(c)** being consistent with the TFL.

The comparison of results from B9-4%-15 to all the else here points to greater importance of cooling from a warmer temperature; namely, the cooling from T_1=-9°C to T_2=-15°C does not have the same 'healing' effect as that from -4°C to -9/-15°C. This may be rather intuitive, if one considers the difference in the ratio T_2/T_1 between them. However, the exact physics behind this remains speculative. One possible factor is the unfrozen water content, w_u. Kasaoka clay's unfrozen water content estimated by Nuclear Magnetic Resonance (NMR) and undrained volume change observation was around 14, 11 and 10% for T=-4, -9 and -15°C, respectively, when frozen from K_0-consolidation at 100kPa. The decrease in w_u, and hence the formation of new pore ice, is greater when cooling occurs from -4°C. However, given that the change of w_u in 10-14% is small relative to the total water content of around 38% in the consolidated specimen, it may not be the sole factor. Another possible factor is the cryogenic suction, which is roughly estimated by 1.2($T_f - T$) (MPa), where T_f (°C) is the freezing temperature (Nishimura and Wang, 2019). The suction increase is linear against the temperature decrease, and it might reinforce the tensile strength. Unfortunately, the macroscopic element tests in this study do not allow individual contribution of these two factors to be assessed. A future study on frozen sand will be informative, because w_u is nearly zero below T_f and barely changes with temperature, therefore isolating the potential suction effect. Similarly, frozen clay with saline pore water has more gradual change of w_u with temperature (e.g. Lyu et al., 2021), possibly making the w_u-effect more visible.

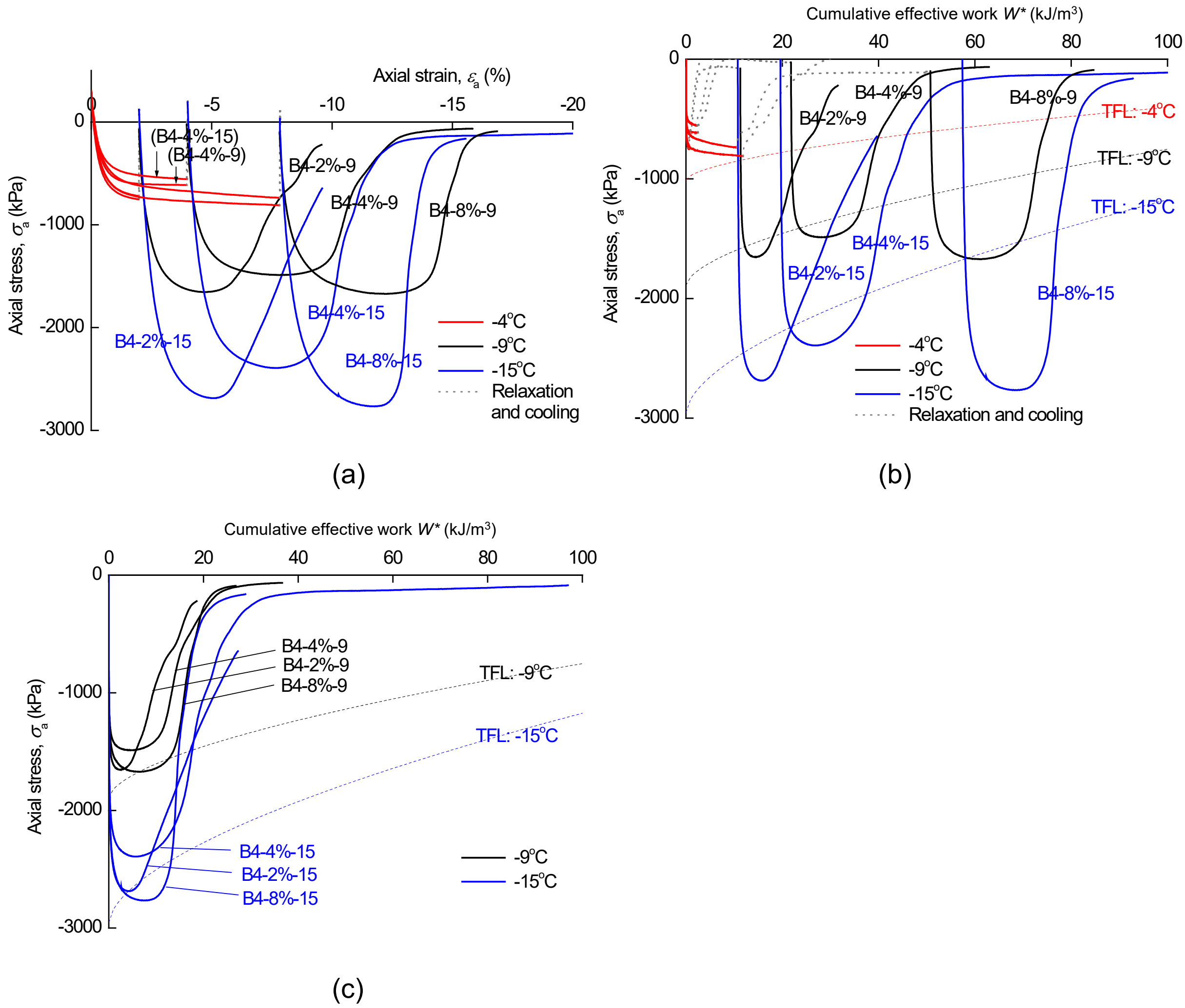

Figure 15: **Tensile behaviour in cases where cooling from -4°C occurred during loading pause: (a) Axial stress-strain, (b) Axial stress-effective work, (c) Axial stress-effective work, with cumulative work** W **and effective work** W^* **reset to zero after cooling**

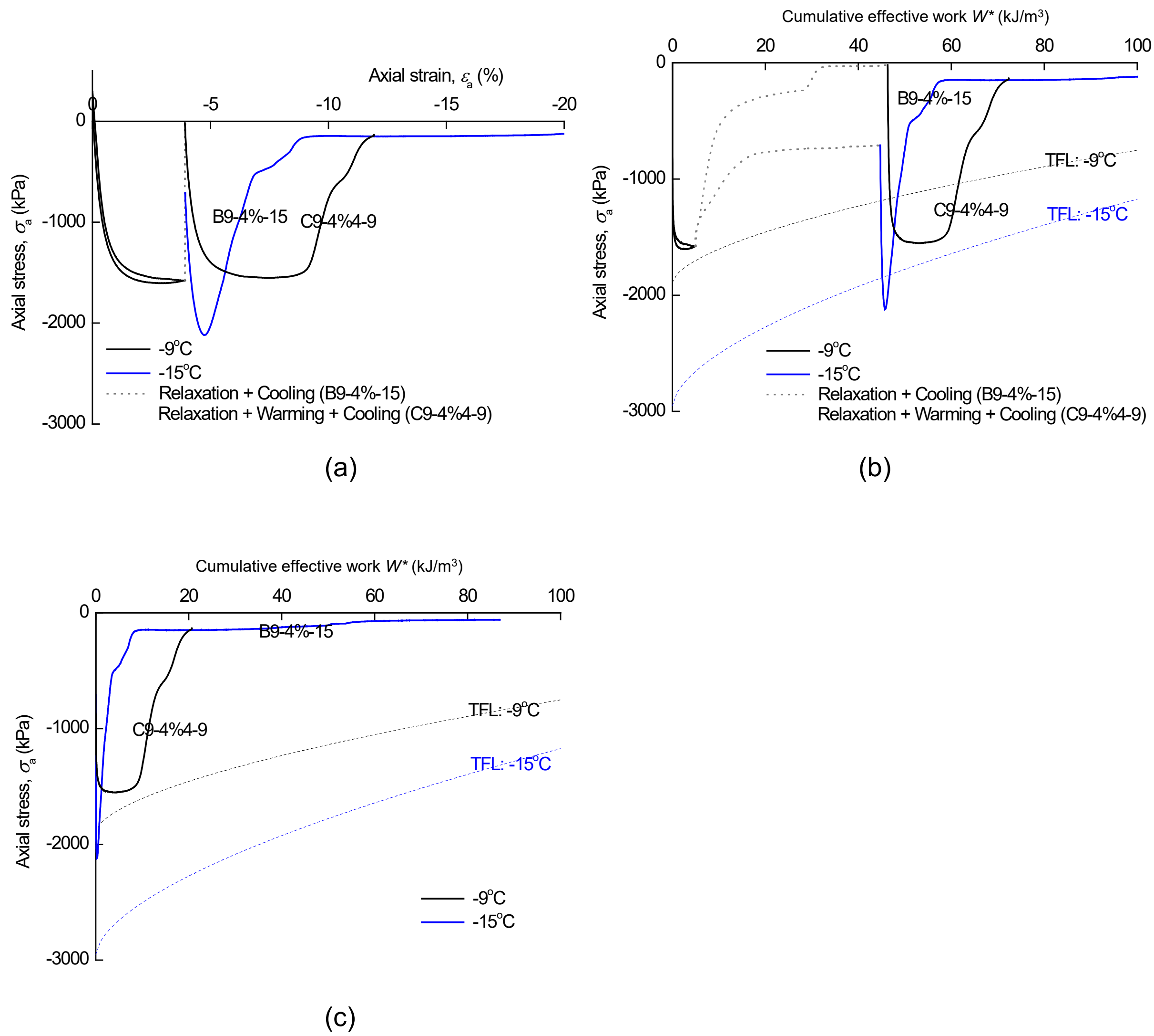

Figure 16: Tensile behaviour in cases where cooling from -9°C (via temporary warming to -4°C in case of C9-4%4-9) occurred during loading pause: (a) Axial stress-strain, (b) Axial stress-effective work, (c) Axial stress-effective work, with cumulative work W and effective work W^* reset to zero after cooling

IMPLICATIONS TO MODELLING AND PRACTICE

The interpretation scheme adopted in this study, combining the delayed tensile-degradation concept and temperature-dependent TFLs, is easy to be implemented in incremental numerical computation. The involved parameters are decay parameter a and those expressing the TFLs geometry. This scheme will provide criteria for tensile failure onset (but not necessarily an absolute state bound, as discussed earlier) against irregular loadings and warming. Existing failure criteria of tensile failure are all history-independent, to the authors' knowledge. In them, the tensile strength is typically given by the power law of strain rate $\dot{\varepsilon}$ (Carbee and Zhu, 1987; Azmatch et al., 2011) or as simple functions of temperature T (Akagawa and Nishisato, 2009). These approaches may work for monotonic strain rates, but the present study demonstrated that this is not the case for non-monotonic cases.

Note that the proposed TFLs are just failure criteria, and not a full constitutive model (i.e. stress-strain model). The deformation analysis still requires a separate elasto-plastic model, with which W and W^* are computed at each step. When the stress $(\sigma_3) - W^*$ relationship hits the TFLs, the tensile failure initiates. The subsequent analysis will depend on engineering decision; one may develop and implement a softening model along the TFLs, or may stop the analysis at this point, concluding that the design is unallowable. For cooling, still more work is necessary to quantify what conditions brings how much 'healing' effect, which apparently cancels the cumulative damage and gives the frozen soil new room for ductile deformation. However, the results in **Figures 15** and **16** reveal that relatively modest cooling can potentially revive the tensile resistance. Observational approach in AGF may therefore be accompanied by additional cooling to warrant extra stability, should a sign of tensile instability be detected during construction. This possibility has been clear for shear (e.g. Wang et al., 2017), but this study demonstrated it for tensile resistance, and tensile ductility too.

Even outside the context of numerical analysis, a $\sigma_a : W^*$ plot (or more generally, $\sigma_3 : W^*$ plot) can be used to interpolate or extrapolate the rate effect. One important lesson from the experimental results is that slower loadings or loading pauses do not lead to subsequent stability against tension, as sometimes observed in shear. The TFL geometry in the $\sigma_a : W^*$ plot implicitly enforces this notion.

Two points are finally to be reiterated. The above modelling concerns only tensile failure, and the simulation of stress-strain curves still requires an auxiliary shear model. A shear model is used to compute the effective shear work, which dictates the evolution of the tensile limit. This may be understood as a kind of shear-tensile unilateral (i.e. shear affecting tension but not the other way around) double-hardening model. The other is that the TFL is not meant to be a stress lower-bound but as an instability condition. Given the potentially grave consequences of tensile failure in AGF, it may be set more conservatively than was in this study.

CONCLUSIONS

This study continued with the first authors' earlier work (Nishimura et al., 2023) on the tensile strength of frozen clay by performing triaxial tension tests, in which the axial total stress σ_a was decreased to negative values while zero or positive lateral total stress was maintained. A particular interest in this study was to understand the tensile strength against different loading rates, and more generally, against irregular loading and temperature changes. The test conditions involved insertion of loading pause(s), temperature increase, decrease or both, and variable loading rates. It was clear that the tensile behaviour reflected not only the contemporary loading rate and temperature, but also their history. Important observations include:

- Faster loading led to greater peak tensile resistance, as in compression. However, unlike in the compression behaviour seen in the literature, faster loading also increased the strain at tensile failure significantly. Different combinations of lateral stress (0-650kPa) and loading rate (0.01-1%/min) resulted in the strain at tensile failure varying as widely as 1-20%.
- Applying loading pauses led to earlier onset of the tensile failure than in monotonic loading. This effect was stronger when the loading pause was applied at a greater strain.
- Once the tensile failure was triggered, speeding the loading up did not bring back the ductility.

One effective way to model the results consistently is introducing the delayed tensile-degradation governed by 'effective' work, W^*, and temperature-dependent Tensile Failure Lines (TFLs) in the σ_a: W^* plot. The shear work input to the frozen clay is converted to W^* by an exponential time-decay function, thus making slower loading and inclusion of loading pauses more prone to effective work accumulation and less resistant to tension. This scheme can be readily implemented to incremental computation. The TFLs are seen to provide consistent criteria for tensile instability against any loading patterns under constant temperature.

The same scheme is also successful in explaining the tensile failure when the frozen clay experienced warming during tension. However, explaining the cases involving cooling required additional consideration. The cooling from -4$^\mathrm{o}$C to -9$^\mathrm{o}$C or to -15$^\mathrm{o}$C apparently cancels almost entirely the accumulated damage, while this effect was limited for cooling from -9$^\mathrm{o}$C to -15$^\mathrm{o}$C.

The insights from this study can be useful directly to numerical modelling. They are encapsulated in the σ_a: W^* plot and TFLs, and these can be used to interpolate or extrapolate the experimental data with limited loading rate conditions too. Exploiting the 'healing' effect by cooling might lead to more adaptive approaches in the observational method in Artificial Ground Freezing (AGF) application.

AKNOWLEDGEMENTS
This study was conducted with JSPS Kakenhi Grants-in-Aid 22H01582 and 25H00748. Francesca Casini's work at Hokkaido University was supported by JSPS Invitational Fellowships for Research (Short-Term) S24022. The authors are grateful for the funding.

APPENDIX: EQUIVALENT HEIGHT OF DUMBBELL-SHAPED SPECIMEN IN AXIAL LOADING

The dumbbell-shaped specimens have stress and strain concentration in their middle, narrower part. The axial stress at this locality can be obtained by dividing the axial force, F, by the middle cross-section area $\pi D_2^2/4$ (see **Figure 3** for dimensions). However, the strain non-uniformity along the specimen axis means that the middle-part strain cannot be simply obtained by dividing the global axial displacement ΔH_1 by either H_1 or H_2. This appendix explains how the equivalent height H_{eq} is deduced such that the local, middle-part strain is obtained as $-\Delta H_1/H_{\mathrm{eq}}$.

The stress dispersion along the specimen axis is assumed to be uniform, given the gentle tapering. The axial stress $\sigma(z)$ at a given height z, is then given as:

$$\sigma(z) = \frac{4F}{\pi D(z)^2} \tag{A1}$$

where $D(z)$ is the specimen diameter at height z. For describing the pre-failure stress-strain relationship during monotonic tension, a hyperbolic model is adopted:

$$\sigma(z) - \sigma_r = q(z) = \frac{q_{\max}}{1+\frac{q_{\max}}{E\varepsilon(z)}} \tag{A2}$$

where $q_{\max}$ is the maximum deviator stress, E is the initial stiffness, and $\varepsilon(z)$ is the axial strain. For given axial force F, the global axial displacement ΔH_1 is calculated as:

$$\Delta H_1 = -\int_0^{H_1} \varepsilon(z)dz = -\int_0^{H_1} \frac{q_{\max} q(z)}{E(q_{\max} - q(z))} dz = \int_0^{L_1} \frac{q_{\max}(4F/\pi D(z)^2 - \sigma_r)}{E(q_{\max} - 4F/\pi D(z)^2 + \sigma_r)} dz \tag{A3}$$

The two model parameters, $q_{\max}$ and E, are quantified by fitting to the experimentally observed global deviator load-displacement curve at each temperature. **Figure A1** shows a typical calibration result. The calibrated model Eq.(A2) represents the true local stress-strain relationship. The equivalent length H_{eq} is then sought such that the $(4F/\pi D(z)^2 - \sigma_r):(-\Delta H_1/H_{\mathrm{eq}})$ relationship agrees with the $q(z):\varepsilon(z)$ relationships from Eq.(A2). **Figure A2** shows that H_{eq}~52mm satisfies this agreement around the failure. This value of H_{eq} was confirmed to work for at all the tested temperatures. The local, middle-part strain in the pre-failure stage can thus be reasonably calculated by dividing the globally measured axial displacement by H_{eq}=52mm.

When a similar analysis is performed by assuming linear elasticity, H_{eq}=75.6mm is calculated for the adopted specimen geometry, irrespective of the assumed stiffness. H_{eq} is much greater than with the non-linear model, as the strain concentration is limited. Given that the response is initially linear, H_{eq} is not constant during tension, but decreases from 75.6mm to around 52mm near failure. However, adopting H_{eq}=52mm is satisfactory in tracking the overall local stress-strain behaviour up to failure as seen in **Figure A2**. When a small-strain stiffness is calculated from the initial part of the response, adopting H_{eq}=75.6mm would be more appropriate.

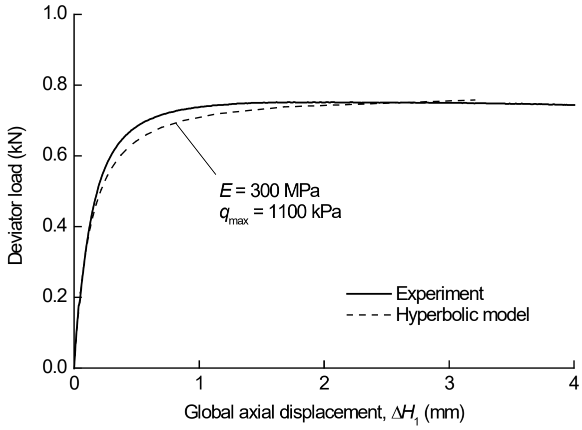

Figure A1: Example of hyperbolic model calibration against experiment (A4-300-0.1)

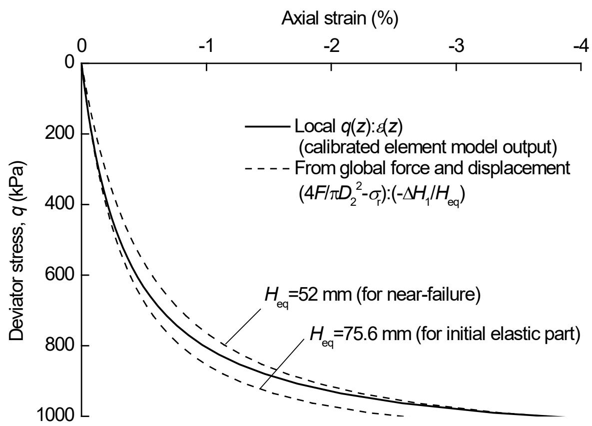

Figure A2: Example of comparison of stress-strain relationships from hyperbolic model and from equivalent height calculation (A4-300-0.1)

REFERENCES

Akagawa, S. and Nishisato, K. (2009) Tensile strength of frozen soil in the temperature range of the frozen fringe. Cold Regions Science and Technology 57 13-22. DOI: 10.1016/j.coldregions.2009.01.002

Azmatch, T. F., Sego, D. C., Arenson, L. U. and Biggar, K. W. (2011) Tensile strength and stress-strain behaviour of Devon silt under frozen fringe conditions. Cold Regions Science and Technology 68 85-90. DOI: 10.1016/j.coldregions.2011.05.002

Casini, F., Guida, G., Restaini, A. and Celot, A. (2023) Water retention curve–based design method for the Artificial Ground Freezing: The Isarco River Underpass Tunnels within the Brenner Base Tunnel Project. Journal of Geotechnical and Geoenvironmental Engineering 149 (3). DOI:

10.1016/j.tust.2020.103534

Eckardt, H. (1982) Creep tests with frozen soils under uniaxial tension and uniaxial compression. The Proceedings of the 4th Canadian Permafrost Conference, Calgary, Alberta, Eds. French, H. M., National Research Council of Canada, Ottawa, Canada 394-405.

Jessberger, H. L. (1981) A state-of-the-art report. Ground freezing: Mechanical properties, processes and design. Engineering Geology 18 (1) 5-30. DOI: 10.1016/B978-0-444-42010-7.50006-2

Jones, J. S. and Brown, R. E. (1978) Soft-ground tunneling by ground freezing: A case history. Transportation Research Record 684, Transportation Research Board, ISSN: 0361-1981, 28-36.

He, P., Zhu, Y. and Cheng G. (2000) Constitutive models of frozen soil. Canadian Geotechnical Journal 37 811-816. DOI: 10.1139/t00-014

Izuta, H., Yamamoto, H. and Ohrai, T. (1988) Mechanical properties of circular slabs of frozen sand clay. Proceedings of the 5th International Symposium o Ground Freezing, Nottingham, UK, Eds. Jones, R., H. and Holden, J. T., Balkema, Rotterdam, The Netherlands 187-192.

Kochi, T., Nishimura, S. and Yamazoe, N. (2025) Thermo-mechanical behaviour of peats under one-dimensional compression. Géotechnique, Ahead of Print. DOI: 10.1680/jgeot.23.00494

Li, K.Q., Yin, Z. H., Yang, Z. H., Liu, Y. (2025) State of the art of mechanical behaviors of frozen soils through experimental investigation. Cold Regions Science and Technology 236 104497. DOI: 10.1016/j.coldregions.2025.104497

Lyu, C., Nishimura, S., Ghoreishian Amiri, S. A., Zhu, F., Eiksund, G. R. and Grimstad, G. (2021) Pore-water pressure development in a frozen saline clay under isotropic loading and undrained shearing. Acta Geotechnica 16 3831～3847. DOI:10.1007/s11440-021-01338-y

Nagai, Y. and Nishimura, S. (2020) The effect of freezing method on frozen clay strength in triaxial compression test. Technical Reports of JGS Hokkaido Branch 60 1-10. https://jgs-hokkaido.org/reports/report-202001/ (in Japanese)

Nishimura, S., Kawasaki, H. and Sato, I. (2023) On limit strength of frozen clay undergoing triaxial tension. Géotechnique 74 (12) 1241-1253. DOI: 10.1680/jgeot.22.00192

Nishimura, S. and Wang, J. (2019) A simple framework for describing strength of saturated frozen soils as multi-phase coupled system. Géotechnique 69 (8) 659-671 DOI: 10.1680/jgeot.17.P.104

Okubo, K., Okamoto, T., Ryokai, K. and Izuta, H. (2000) Evaluation of countermeasures for 1.10 MPa frost expansion pressure using a new measurement system. Proceedings of the 5th International Symposium o Ground Freezing, Louvain-la-Neuve, Belgium, Eds. Thimus, J.-F., Balkema, Rotterdam, The Netherlands 299-303.

Parameswaran, V. R. (1980) Deformation behaviour and strength of frozen sand. Canadian Geotechnical Journal 17 (1) 74-88. DOI: 10.1139/t80-007

Schindler, U., Chrisopoulos, S., Cudmani, R. and Vogt, S. (2025) Experimental and numerical investigations on the multi-stage creep behavior of frozen sand under stepwise loading and

unloading. Cold Regions Science and Technology 231, 104419. DOI: 10.1016/j.coldregions.2025.104419
Tatsuoka, F., Ishihara, M., di Benedetto, H. and Kuwano, R. (2002) Time-dependent shear deformation characteristics of geomaterials and their simulation. Soils and Foundations 42 (2) 103-129. DOI: 10.3208/sandf.42.2_103
Viggiani, G. M. B., Casini, F., Winter, M. G., Smith, D. M., Eldred, P. J. L. and Toll, D. G. (2015) Artificial ground freezing: from applications and case studies to fundamental research. Proceedings of the 16th ECSMGE Geotechnical Engineering for Infrastructure and Development, ICE Publishing 65–92. DOI:10.1680/ecsmge.60678
Wang, J., Nishimura, S. and Tokoro, T. (2017) Laboratory study and interpretation of mechanical behavior of frozen clay through state concept. Soils and Foundations 57 (2) 194-210. DOI: 10.1016/ j.sandf.2017.03.003
Xu, X., Dong, Y. and Fana, C. (2015) Laboratory investigation on energy dissipation and damage characteristics of frozen loess during deformation process. Cold Regions Science and Technology 109 1-8. DOI: 10.1016/j.coldregions.2014.09.006
Xu, X., Wang, Y., Yina, Z. and Zhang, H. (2017) Effect of temperature and strain rate on mechanical characteristics and constitutive model of frozen Helin loess. Cold Regions Science and Technology 136 44-51. DOI: 10.1016/j.coldregions.2017.01.010
Yamamoto, Y. and Springman, S. M. (2017) Three- and four-point bending tests on artificial frozen soil samples at temperature close to 0 °C. Cold Regions Science and Technology 134 20-32. DOI: 10.1016/j.coldregions.2016.11.003
Zhou, G., Hu, K., Zhao, X., Wang, J., Liang, H. and Lu, G. (2015) Laboratory investigation on tensile strength characteristics of warm frozen soils. Cold Regions Science and Technology 113 81-90. DOI: 0.1016/j.coldregions.2015.02.003
Zhou, Z., Ma, W., Zhang, S., Cai, C., Mu, Y. and Li, G. (2017) Damage evolution and recrystallization enhancement of frozen loess. International Journal of Damage Mechanics 27(8) 1131-1155. DOI: 10.1177/1056789517731138
Zhu, Y. and Carbee, D. L. (1985) Strain rate effect on the tensile strength of frozen silt. The Proceedings of the 4th International Symposium on Ground Freezing, Sapporo, Japan, Eds. Kinoshita, S. and Fukuda, M., Balkema, Rotterdam, The Netherlands 153-157.
Zhu, Y. and Carbee, D. L. (1987) Tensile strength of frozen silt. CRREL Report 87-15. 23p.

LIST OF NOTATIONS

a: Decay parameter for converting W to W^*l

D_1, D_2: Diameters of the end and middle parts of the specimen

H_1, H_2: Total and middle part heights of the specimen

H_{eq}: Equivalent height of the specimen

p, p': Total and effective mean effective stresses, respectively

p_c': Effective mean effective stress at consolidation

p_f: Total mean effective stress after freezing and before extension

q: Deviator stress (=radial stress – axial stress)

q_{max}: Maximum deviator stress

t and τ: Time

T: Temperature

W: Work input to soil

W^*: Effective work

w_u: (Gravimetric) unfrozen water content

ε_1, ε_3: Major and minor principal strains, respectively

$\dot{\varepsilon}_a$: Axial strain rate (absolute value)

ε_a, ε_r: Axial and radial strains (=ε_3 and ε_1, respectively)

ε_{ap}: Axial strain at loading pause

σ_1, σ_3: Major and minor principal stresses, respectively

σ_a, σ_r: Axial and radial stresses (=σ_3 and σ_1, respectively)

AGF: Artificial Ground Freezing

TFL: Tensile Failure Line